

# Impact of Numerical Methods in Thermal Modeling of Li-Ion Batteries on Temperature Distribution and Computation Time

Zoltan Veszelka,\* Oliver Queisser, Martin Gontscharow, Thomas Wetzel, and Willy Dörfler

Thermal battery modeling is important for further battery development and optimization. The temperature strongly influences the performance and aging behavior. In the cell stack, electrochemical processes take place resulting in a large amount of heat release, which, in turn, affects the temperature distribution. Therefore, the main focus is on the cell stack, the most complex structure inside the cell. In particular, the discontinuous and anisotropic material properties represent a major challenge for simulations due to the layering. This work proposes self-developed methods, based on the Finite Volume Method and the Finite Element Method, taking on these challenges. First, for both methods the functionality is verified and numerical convergence is validated. These, and also classical methods, are compared based on test problems with a known analytical solution in view of numerical errors as well as computing time. It is found that their accuracy and efficiency depends strongly on the specific problem, which makes their numerical investigation necessary and inevitable. Second, the methods are evaluated on a specific battery problem. Their results are plausible and correspond to the physical phenomena.

## 1. Introduction

Li-ion battery cells are in the focus of social interest due to their wide field of application in all kinds of mobile devices as well as electric mobility.

The temperature has large impact on the performance and aging behavior of battery cells.<sup>[1,2]</sup> Inhomogeneities in

the temperature field lead accordingly to an inhomogeneous current distribution and thus again to changes in the heat release which in interaction with the thermal boundary condition results in a more pronounced inhomogeneous temperature distribution.<sup>[3]</sup>

Typically, thermal battery models are developed in 2D or 3D.<sup>[4]</sup> As the thermal processes are described by partial differential equations (PDE), these models are mostly based on numerical methods such as the Finite Volume Method (FVM) or the Finite Element Method (FEM).<sup>[4,5]</sup> A battery cell consists of a large number of thin layers in a cell stack or jelly roll. In common approaches, these thin layers are resolved by the grid. This results in a very fine grid and leads to a large number of degrees of freedom which, in turn, results in high computing times. For that reason individual layers<sup>[6,7]</sup> or even, as

mentioned before, the whole cell stack are homogenized.<sup>[8,9]</sup> The full homogenization of the stack to one block with a uniform set of material properties represents the most widely spread approach of modeling such thermal battery problems. As shown in Queisser et al.,<sup>[7]</sup> the accuracy of the temperature field of this fully homogenized (FH) approach is poor. Thus, there is the need to find other approaches. One would be to lessen computing time by dimensional reduction, but it has already been shown that a 3D model depicts the temperature distribution best by far and should therefore be addressed in the model development.<sup>[4]</sup> Therefore, either the more detailed resolution of the stack structure, e.g., using a partial homogenization (PH),<sup>[6,7]</sup> the full resolution of each layer,<sup>[7,10]</sup> or new mathematical approaches are necessary.

These mathematical approaches can be either analytical or numerical. One of the most used analytical methods is the asymptotic homogenization, which is applied by Hunt et al.<sup>[11]</sup> and Hennessy et al.<sup>[12]</sup> for electrochemical-thermal battery modeling. They identified the characteristic length scales of the battery, such as the particle called microscale, the electrode called mesoscale, and the cell called macroscale, and, starting at the microscale, they expanded the solution in a power series with regard to this length scale parameters. By matching powers of this parameters, they derived analytical equations for the mesoscale and then for the macroscale variables.

Z. Veszelka, M. Gontscharow, Prof. W. Dörfler  
Institute of Applied and Numerical Mathematics  
Karlsruhe Institute of Technology (KIT)  
Englerstr. 2, Karlsruhe 76131, Germany  
E-mail: zoltan.veszelka@kit.edu

O. Queisser, Prof. T. Wetzel  
Institute of Thermal Process Engineering  
Karlsruhe Institute of Technology (KIT)  
Kaiserstr. 12, Karlsruhe 76131, Germany

 The ORCID identification number(s) for the author(s) of this article can be found under <https://doi.org/10.1002/ente.202000906>.

© 2021 The Authors. Energy Technology published by Wiley-VCH GmbH. This is an open access article under the terms of the Creative Commons Attribution-NonCommercial License, which permits use, distribution and reproduction in any medium, provided the original work is properly cited and is not used for commercial purposes.

DOI: 10.1002/ente.202000906

Another analytical approach is used by Kim et al.<sup>[13]</sup> They applied a multiscale, multidimensional (MSMD) approach to an electrochemical–thermal battery model. Therein, they solved the characteristic coupled equations on every scale and exchanged parameters between the scales by averaging the solutions.

Numerical homogenization methods follow another approach. Their goal is to solve the multiscale PDE without analytically deriving a homogenized equation for the meso- and macroscale. Keeping sufficient accuracy they do not resolve, but neither neglect, the fine scales. Thereby, at least two or even three spatial scales can be connected. Examples for such methods are the Multiscale Finite Element Method<sup>[14]</sup> and the Reduced Basis Method.<sup>[15]</sup>

A new approach to the application to battery simulation models is the Heterogeneous Multiscale Method (HMM) which is investigated in this work in more detail. Engquist<sup>[16]</sup> first introduced this method and reviewed it later.<sup>[17]</sup> It is a general mathematical framework for solving various multiscale problems. The scales, typically a microscale and a macroscale, are coupled via mathematical techniques. These constrain the microscale solutions so that they are consistent to the local macroscopic state. Abdulle and Schwab<sup>[18]</sup> use FEM on both scales for a diffusion problem on a rough surface, which leads to the Finite Element Heterogeneous Multiscale Method (FE-HMM). Later Abdulle<sup>[19]</sup> reviewed and extended it to standard elliptic problems and discussed the error analysis of the method. So far the method has been applied to various problems, e.g., parabolic problems<sup>[20]</sup> or to nonlinear monotone parabolic problems.<sup>[21]</sup>

It is noticeable that there are many different variants for the mapping of peripheral components, e.g., tabs or housing, in models.<sup>[4,8]</sup>

Up to now, we know of no publication that, for the case of thermal modeling of battery cells, evaluates the errors with respect to the spatial and temporal discretization.

In this work, different methods derived from the software OpenFOAM, which uses FVM, and from the finite element library deal.II, which uses FEM, are applied to a thermal battery model. This model is introduced in Section 2. On the one hand, for the FVM a new method is developed that will be introduced in Section 3.2. On the other hand, for the FEM in Section 4.2, an existing homogenization method is newly applied and further developed to such a problem. Both methods are extended in regard to deal with anisotropy, nonlinearity, the ability to release heat, and the discontinuity of the material properties. In addition, already existing standard methods were used for comparison. These are described in Section 3.1 and 4.1, respectively. Then in Section 5.1 and 5.2 the methods are applied to appropriate test problems with known analytical solution to evaluate the errors and computing times. In Section 5.3, the battery model is investigated using these methods under various boundary conditions. Finally in Section 6, a summary and concluding remarks about future work and possible challenges are given.

## 2. Thermal Model

### 2.1. Thermal Transport

Thermal investigations of simulation models for batteries focus on the analysis of the temperature distribution and thus the

solution of the transient, inhomogeneous heat transport equation. Inside a 3D bounded domain  $\Omega := [0 \text{ m}, 0.0395 \text{ m}] \times [0 \text{ m}, 0.112 \text{ m}] \times [0 \text{ m}, 0.0074639 \text{ m}] \subset \mathbb{R}^3$ , which depicts the battery, the temperature field  $T: \mathbb{R}_{\geq 0} \times \mathbb{R}^3 \rightarrow \mathbb{R}_{\geq 0}$ ,  $t, x \mapsto T(t, x)$ , represents the solution of the heat equation (Equation (1)). The temperature  $T$  depends on the time variable  $t \geq 0$  and the spatial quantity  $x$  in  $\Omega$ . As the temperature is defined in Kelvin,  $T$  maps into the nonnegative numbers ( $\mathbb{R}_{\geq 0}$ ). The further parameters are defined in the same way. Two common approaches to solve this equation are the FVM, explained in more detail in Section 3, and the FEM, which will be described in Section 4. All dependencies that are taken into account are shown in the initial-boundary value problem

$$\rho(x) \partial_t (c_p(x, T) T(t, x)) = \nabla \cdot (\lambda(x, T) \nabla T(t, x)) + \dot{Q}_{\text{src}}'''(x) \quad (1)$$

Here  $\rho: \Omega \rightarrow \mathbb{R}_{>0}$  denotes the *density*,  $c_p: \Omega \times \mathbb{R}_{>0} \rightarrow \mathbb{R}_{>0}$  the *specific heat capacity*,  $\lambda: \Omega \times \mathbb{R}_{>0} \rightarrow \mathbb{R}_{>0}^{3 \times 3}$  the *thermal conductivity*, and  $\dot{Q}_{\text{src}}''' : \Omega \rightarrow \mathbb{R}$  the *volumetric heat source*. The apostrophes denote normalization of the quantity to the spatial dimension. The normalization in terms of area is indicated by two apostrophes, in terms of volume by three. Apart from their dependency on temperature and, especially for the thermal conductivity, on the transport direction, the coefficients are material dependent and therefore they are often discontinuous. This characteristic will be investigated in Section 5.2, in which the convergence behavior of different methods is discussed.

As initial condition, a uniform temperature  $T_{\text{init}}$  is set to 298 K. The heat generation is calculated to an average value of 3 W for the whole cell from experimental data acquired for a pouch cell at a 3 C discharge cycle. It is then evenly distributed to the active material layers. It is applied to the active material parts of the cell and it is therefore discontinuous as well because in the left components the heat release is set to 0 W. Bernardi et al.<sup>[22]</sup> present more detailed information about the dependencies and thus the equations for calculating the heat release.

### 2.2. Thermal Boundary Conditions

There are three typical boundary conditions for thermal problems [<sup>[23]</sup> Section E2]. The first one is a Dirichlet boundary condition, where a temperature  $T_{\text{BC}}$  can be set as

$$T(t, x) = T_{\text{BC}}(t, x) \quad \forall t > 0, x \in \Gamma_{\text{D}} \quad (2)$$

with the Dirichlet boundary  $\Gamma_{\text{D}} \subseteq \partial\Omega$ . Second, a Neumann boundary condition specifies a heat flux  $\dot{Q}_{\text{BC}}''$  normal to the boundary as

$$-\lambda \partial_n T(t, x) = \dot{Q}_{\text{BC}}''(x) \quad \forall t > 0, x \in \Gamma_{\text{N}} \quad (3)$$

with the Neumann boundary  $\Gamma_{\text{N}} \subseteq \partial\Omega$  and the normal derivative  $\partial_n T$ . Noteworthy, through a perfect isolated, called adiabatic, system no heat is transferred. Therefore, it is determined by a zero Neumann boundary condition. Third, a Robin boundary condition represents a combination of the previous two boundary conditions, in which the normal gradient of the temperature to the boundary is set to Newton's cooling law as

$$-\lambda \partial_n T(t, x) = \alpha(T(t, x) - T_{BC}(t, x)) \quad \forall t > 0, x \in \Gamma_R \quad (4)$$

where  $\alpha$  is the heat transfer coefficient and  $\Gamma_R \subseteq \partial\Omega$  is the Robin boundary. These boundary conditions can also be combined, and then each one is only valid on a part of the boundary.

### 2.3. Model Geometry and Parameterization

The geometry of a pouch cell is composed of different stacked layers, the anode and cathode tab as well as a casing, which is made of a separator and an aluminum compound foil. The main focus of these investigations is the layered stack. Due to that, all remaining components are not considered further. In the stack, unit cells consisting of a cathode current collector (CCC), an active material (AM) layer, and an anode current collector (ACC) are piled. Opposite to the common approaches of homogenizing the whole stack to one FH block, Queisser et al.<sup>[7]</sup> describe an approach of PH, which is used to homogenize the three layers anode and cathode coating as well as separator to only one remaining layer. Using this homogenization approach, the total number of layers in the stack of the chosen cell can be reduced by almost one half and so 133 layers remain from 265 layers in the fully resolved cell. In **Figure 1**, a battery cell consisting of 17 layers is visualized. The thermal conductivity in  $z$ -direction is shown in **Figure 2**. Note that the visualization tool shows a continuous linear interpolation of the discontinuous function.

In the next step, the material layers in the model are parameterized using the data shown in **Table 1**.

## 3. Finite Volume Solvers

In Supporting Information A, the derivation of the FVM for the linear problem—i.e. for temperature independent  $\lambda$  and  $c_p$ —of Equation (1) was shown. In the next sections, two methods based on this derivation will be introduced. The first one is a standard OpenFOAM solver and the second one is a self-developed variant.

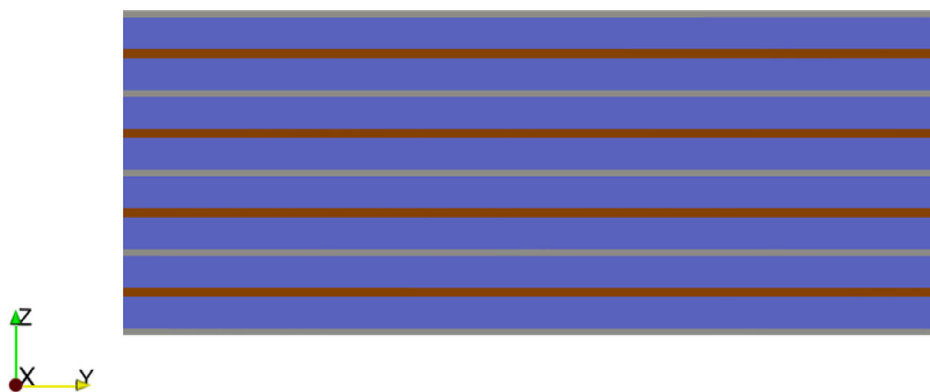


**Figure 1.** Model geometry with 17 layers of cell stack of the battery cell with resolved cathode current collector (gray), anode current collector (copper), and homogenized active material (blue).

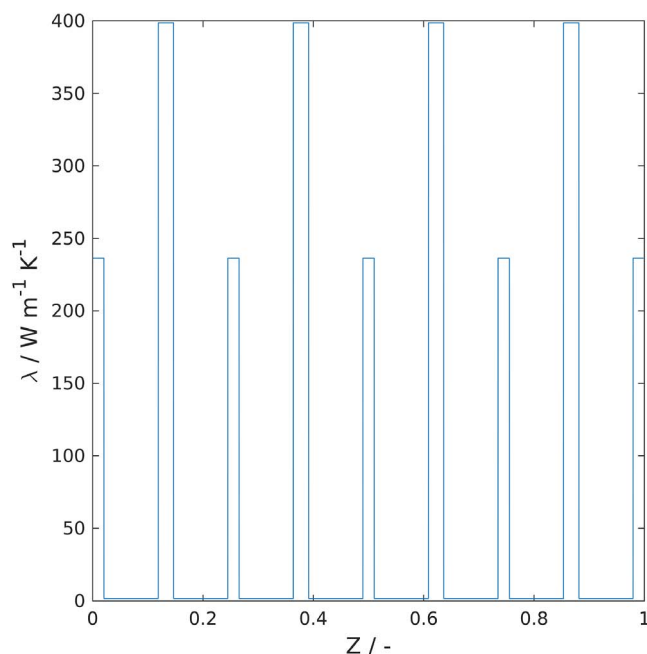


**Figure 2.** Schematic illustration of the thermal conductivity  $\lambda$  in  $z$ -direction for the 17 layers shown in Figure 1.

**Table 1.** Material properties of the layers in the cell stack from Queisser et al.<sup>[7]</sup>

	Density $\rho$ [ $\text{kg m}^{-3}$ ]	Specific heat capacity $c_p$ [ $\text{J kg}^{-1} \text{K}^{-1}$ ]	Thermal conductivity $\lambda_{\parallel}$ [ $\text{W m}^{-1} \text{K}^{-1}$ ]	Thermal conductivity $\lambda_{\perp}$ [ $\text{W m}^{-1} \text{K}^{-1}$ ]
ACC	8710.2	384.65	398.71	398.71
CCC	2706.77	897.8	236.3	236.3
AM	2094.302	1010.119	1.741	0.683

### 3.1. chtMultiRegionFoam

This standard OpenFOAM solver is capable of solving either steady-state or transient heat transfer problems consisting of

both solid and/or fluid regions interacting with each other.<sup>[24]</sup> Therefore, the consequence is an extensive communication mechanism to even solve boundary layers in a fluid. Due to that each domain is calculated separately exchanging the values of the unknowns via specific interface conditions. In addition, so-called nOuterCorrectors are implemented denoting the number of cycles repeating a loop around the whole solving process within one time step. This is comparable with an iteration loop considering the pressure correction using the PIMPLE algorithm, which is a combination of SIMPLE and PISO algorithms<sup>[25]</sup>, Section 7]. An advantage of this solver is the applicability to such a problem with discontinuous material properties, even when some features remain unused. This refers for the thermal battery model in particular to the regions. Only solid regions are used, but the nOuterCorrectors are still necessary through the discontinuity due to the coupling of the many layers and thus many regions.

### 3.2. layeredLaplacianFoam

In this section, the further developed solver layeredLaplacianFoam based on the standard OpenFOAM solver laplacianFoam will be introduced. This new solver is capable of solving the nonlinear version of Equation (1) without splitting the domain into subdomains for each component, meaning the domain is considered as a whole. The coefficients are defined with the help of functions that depend on the spatial coordinates. The standard solver is able to solve equations of the form

$$\partial_t T - \nabla \cdot (D_T \nabla T) = S_T \quad (5)$$

$D_T$  and  $S_T$  are the constant scalar diffusion coefficient and the source term, respectively. For a detailed description of the solver, see the study by Greenshields.<sup>[24]</sup>

To arrive at layeredLaplacianFoam, LaplacianFoam will be modified and further developed because it only solves problems of the form of Equation (5). In the first step,  $D_T$  and  $S_T$  are replaced by a  $T$ -dependent variable that incorporates  $\rho$  and  $c_p$ , too. So  $D_T$  will be replaced by

$$\kappa(T) := \frac{\lambda(T)}{\rho c_p} \quad (6)$$

and  $S_T$  by

$$\beta := \frac{\dot{Q}_{src}'''}{\rho c_p} \quad (7)$$

These quotients are well defined because the density and the heat capacity are positive for each layer (cf. Table 1). Because they are moreover scalar constants in each layer (cf. Table 1),  $\kappa$  can be written inside the divergence operator.

The next step is to take care of the coefficients. Here, Equation (1) is solved with constant scalar density, heat capacity, and source term in each layer. The coefficient  $\rho$  is of the form

$$\rho(x) = \begin{cases} \rho_{ACC}, & x \in ACC \\ \rho_{CCC}, & x \in CCC \\ \rho_{AM}, & x \in AM \end{cases} \quad (8)$$

and the same kind of definition is used for the heat capacity  $c_p$  and the heat source  $\dot{Q}_{src}'''$ . The heat conductivity is defined layerwise, too. In addition to its nonlinearity, it is anisotropic as well. In this case, the coefficient has in each layer the form

$$\lambda(T) = \begin{pmatrix} \lambda_x(T) & 0 & 0 \\ 0 & \lambda_y(T) & 0 \\ 0 & 0 & \lambda_z(T) \end{pmatrix} \quad (9)$$

The nonlinear coefficient  $\lambda_x$  has in each layer the form

$$\lambda_x = \lambda_{x,0} + \lambda_{x,1}T + \lambda_{x,2}T^2 + \dots + \lambda_{x,7}T^7 \quad (10)$$

$\lambda_y$  and  $\lambda_z$  are defined analogously. In combination, this results in a nonlinear polynomial in  $T$  in each component of the anisotropic tensor for  $\lambda$ .

Next, an additional data file named layerProperties is created that consists of all important parameter of the different layers, such as thickness, density, heat capacity, coefficients of the nonlinear and/or anisotropic heat conductivity, and the order of the layers. The solver reads this file at the beginning and uses the data to compute the coefficients for Equation (1) as functions of the spatial variable.

Therefore, it is necessary to assign each individual point to a specific layer. Using a simple algorithm, the solver sums up the thicknesses of the layers in the correct order until the  $z$ -coordinate of the point is reached and it returns the appropriate layer. This algorithm is then applied to the centers of the cells and the coefficients for the whole mesh are defined. This results in coefficients of the form shown in Equation (8).

The application to the cell centers is sufficient because, as described at Supporting Information A, the OpenFOAM solver uses the one point Gauss quadrature for numerical integration and thus one value per cell is enough.

In the last step, the nonlinearity is resolved. As the initial solver laplacianFoam only operates with linear problems, a linearized approach has to be applied. Here,  $\kappa(T)$  is evaluated at time  $t_n$  which leads to the linear equation

$$\frac{T^{n+1} - T^n}{\Delta t} - \nabla \cdot (\kappa(T^n) \nabla T^{n+1}) = \beta \quad (11)$$

for  $T^{n+1}$ . This equation is solved as described in Supporting Information A.

## 4. Finite Element Solvers

In the following we will apply the FEM to Equation (1)

$$\rho(x) \partial_t (c_p(x, T) T(t, x)) = \nabla \cdot (\lambda(x, T) \nabla T(t, x)) + \dot{Q}_{src}'''(x) \quad (12)$$

This standard derivation is presented in Supporting Information B for convenience. In the next sections, two methods based on this derivation will be introduced. The first one is a standard higher order FEM and the second one is a numerical homogenization method.

#### 4.1. Higher Order FEM

In the case of higher order finite elements, the solution is approximated by higher order polynomials on each cell of the decomposition of the domain, in contrast to constants as in the FVM. This leads to higher accuracy for the same resolution of the grid.

At the end of Supporting Information B, the bilinear form (18) and the linear form (19)

$$B(T^{n+1}, \varphi) := \int_{\Omega} \rho \frac{c_p(T^{n+1})T^{n+1} - c_p(T^n)T^n}{\Delta t} \varphi dx + \int_{\Omega} \lambda(T^{n+1}) \nabla T^{n+1} \cdot \nabla \varphi dx \quad (13)$$

$$F(\varphi) := \int_{\Omega} \dot{Q}_{src}''' \varphi dx \quad (14)$$

were derived, but the space  $\mathcal{V}$  was not further specified. In this section, Equation (1) will be solved using the finite element spaces  $\mathcal{V}^p(\mathcal{T}_h) := \{\varphi^h \in \mathcal{H}^1(\Omega) : \varphi|_K \in \mathcal{Q}_p(K) \forall K \in \mathcal{T}_h\}$  of order  $p \in \{1, 2, 3\}$  over an admissible decomposition  $\mathcal{T}_h$  of  $\Omega$  with step size  $h$ , see [26], Section 2.5]. Here,  $\mathcal{H}^1(\Omega)$  is the Sobolev space of order 1, see [27], Section 2.4], and  $\mathcal{Q}_p(K)$  is the space of polynomials with degree at most  $p$  in each coordinate variable on the quadrilateral  $K$ , if  $\Omega \subset \mathbb{R}^2$  and on the cuboid  $K$ , if  $\Omega \subset \mathbb{R}^3$ . This choice for the decomposition is made because the finite element library *deal.II* is used that is based on decompositions into quadrilaterals and cuboids, respectively.

As stated in Supporting Information B, Equation (17)

$$\int_{\Omega} \rho \frac{c_p(T^{n+1})T^{n+1} - c_p(T^n)T^n}{\Delta t} \varphi dx + \int_{\Omega} \lambda(T^{n+1}) \nabla T^{n+1} \cdot \nabla \varphi dx = \int_{\Omega} \dot{Q}_{src}''' \varphi dx \quad \forall \varphi \in \mathcal{V} \quad (15)$$

is solved with the undamped Newton method, see [28], Section 14.2.7]. Defining  $\partial_T B(T_k^{n+1,h}, \varphi^h)$  as the derivative of  $T \mapsto B(T, \varphi^h)$  with respect to  $T$  at  $T_k^{n+1,h}$ , the actual Newton iterate, the equation for the Newton update  $\delta T_{k+1}^{n+1,h}$  reads

$$\partial_T B(T_k^{n+1,h}, \varphi^h) [\delta T_{k+1}^{n+1,h}] = -B(T_k^{n+1,h}, \varphi^h) + F(\varphi^h) \quad \forall \varphi^h \in \mathcal{V}^h \quad (16)$$

Then  $T_{k+1}^{n+1,h} := T_k^{n+1,h} + \delta T_{k+1}^{n+1,h}$  and  $T^{n+1,h} := T_{k+1}^{n+1,h}$  is defined when  $\delta T_{k+1}^{n+1,h}$  is sufficiently small.

In the next step,  $\delta T_k^{n+1,h} = \sum_{i=1}^M T_i^{n+1} \varphi_i^{p,h}$  is defined using the finite element basis functions  $\varphi_i^{p,h} \in \mathcal{V}^p$  and uniquely determined coefficients  $T_i^{n+1} \in \mathbb{R}$ ,  $i = 1, \dots, M$ . This is inserted in Equation (16) and for  $\varphi^h = \varphi_i^{p,h}$ ,  $i = 1, \dots, M$ ,  $\bar{T}^{n+1} := (T_1^{n+1}, \dots, T_M^{n+1}) \in \mathbb{R}^M$  and  $A \in \mathbb{R}^{M \times M}$  the linear system

$$A \bar{T}^{n+1} = F \quad (17)$$

with

$$A_{ij} = \partial_T B(T_k^{n+1,h}, \varphi_j^{p,h}) [\varphi_i^{p,h}] = \frac{1}{\Delta t} \int_{\Omega} \rho c_p'(T_k^{n+1,h}) T_k^{n+1,h} \varphi_i^{p,h} \varphi_j^{p,h} dx + \frac{1}{\Delta t} \int_{\Omega} \rho c_p(T_k^{n+1,h}) \varphi_i^{p,h} \varphi_j^{p,h} dx + \int_{\Omega} \lambda'(T_k^{n+1,h}) \varphi_i^{p,h} \nabla T_k^{n+1,h} \cdot \nabla \varphi_j^{p,h} dx + \int_{\Omega} \lambda(T_k^{n+1,h}) \nabla \varphi_i^{p,h} \cdot \nabla \varphi_j^{p,h} dx \quad (18)$$

and

$$F_i = -B(T_k^{n+1,h}, \varphi_i^{p,h}) + F(\varphi_i^{p,h}) = - \int_{\Omega} \rho \frac{c_p(T_k^{n+1,h})T_k^{n+1,h} - c_p(T_k^{n,h})T_k^{n,h}}{\Delta t} \varphi_i^{p,h} dx - \int_{\Omega} \lambda(T_k^{n+1,h}) \nabla T_k^{n+1,h} \cdot \nabla \varphi_i^{p,h} dx + \int_{\Omega} \dot{Q}_{src}''' \varphi_i^{p,h} dx \quad (19)$$

follows. The integrals are computed with an appropriate Gauss quadrature rule and the linear system is solved with the Conjugate Gradient (CG) algorithm, see [28], Section 11.3.4].

#### 4.2. FE-HMM

As mentioned in the first part of Section 4, Equation (1) is solved with a numerical homogenization method. This means in the context of multiscale methods, that no analytically homogenized equation is derived. The actual multiscale PDE is solved, but the solution converges to the solution of the, in mathematical sense, analytically homogenized equation,[29] i.e. to a problem that has the same structure, but with coefficients that do not depend on the microscale variable.

In this work, the FE-HMM, a general mathematical framework for solving various multiscale problems is used. It uses finite elements to realize the concept of the HMM.[16,17] The idea is that the missing data on the macroscale are approximated by the solution of appropriate microproblems on the microscale. These data are in the case of the battery the homogenized heat capacity and hat conductivity. The two scales are coupled via mathematical techniques that assign the microproblems to the macroproblem in a consistent way. The choice of the methods on the different scales and the coupling between them are problem dependent and determine the exact method. For this approach, the FEM, the Finite Difference Method, or the discontinuous Galerkin method can be used. A reconstruction operator or appropriate boundary conditions are examples for the coupling, see [16], Section 2.2] and [19], Section 3.2], respectively.

As mentioned earlier, the FEM is chosen on both scales, which leads to the FE-HMM. It was first introduced by Abdulle in the study by Abdulle and Schwab[18] and was reviewed and extended in the study by Abdulle.[19] Since then, it has been applied to various problems, among others, to parabolic problems in the study by Ming and Zhang[20] or to nonlinear monotone parabolic problems in the study by Abdulle and Huber.[21] Later, the method applied to quasilinear problems described in the study by Abdulle and Vilmart[30] will be extended to such problems with multiple discontinuous multiscale coefficients. The coupling of

the two scales in the FE-HMM is realized through appropriate boundary conditions, i.e. the boundary conditions of the microproblems are derived from functions on the macroscale.

In the next sections, the main components of FE-HMM will be described based on [30], Section 2] and [31], Section 1.2]. Thereby, the application to the battery problem is directly considered.

#### 4.2.1. Quadrature Formulas

The most important component of the method is the quadrature formula. On one side, as mentioned in Section 3, they are used for the numerical integration of the weak forms—for the macro- and microproblems—and on the other side the quadrature points will be the centers of the microdomains where the microproblems are solved. As the problem is implemented in *deal.II* which works with quadrilateral elements, let  $\hat{K}$  be the reference element of quadrilateral type. For a quadrature formula  $\{\hat{x}_j, \hat{\omega}_j\}_{j=1}^J$  with quadrature points  $\hat{x}_j \in \hat{K}$  and quadrature weights  $\hat{\omega}_j, j = 1, \dots, J$ , the following assumptions are made

$$\hat{\omega}_j > 0, j = 1, \dots, J, \text{ and } \sum_{j=1}^J \hat{\omega}_j |\nabla \hat{z}(\hat{x}_j)|^2 \geq C \|\nabla \hat{z}\|_{L^2(\hat{K})}^2 \quad (20)$$

$$\forall \hat{z} \in Q_p(\hat{K}) \text{ and some } C > 0$$

$$\int_{\hat{K}} \hat{z}(x) dx = \sum_{j=1}^J \hat{\omega}_j \hat{z}(\hat{x}_j) \quad (21)$$

$$\forall \hat{z} \in Q_q(\hat{K}) \text{ for } q = \max(2p - 1, p + 1)$$

These assumptions guarantee that the discrete system is invertible and that integrals over polynomials up to order  $q$  are integrated exactly. In this way, the optimal convergence rates for the FEM with numerical integration are assured. For the macroproblem, as well as for the microproblem, the Gauss quadrature with two quadrature points in each coordinate direction is chosen. In this way, bilinear functions can be exactly integrated and that will be sufficient for the application. For the reference quadrilateral  $\hat{K} = [-1, 1]^2$  in two space dimensions, the quadrature points are  $[\pm 1/\sqrt{3}, \pm 1/\sqrt{3}]$  and all weights are equal to 1. The left and right part of **Figure 3** show how the points are positioned in a macro- and microelement, respectively.

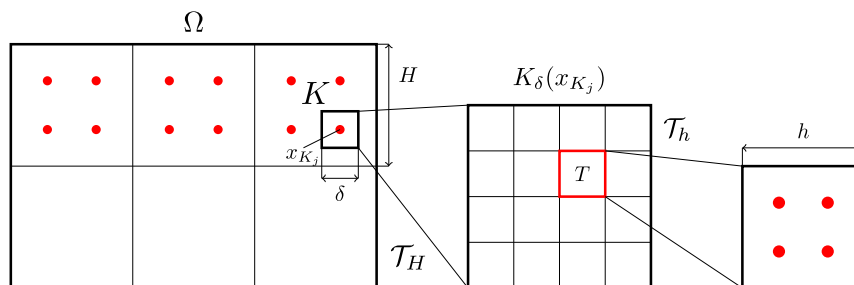


**Figure 3.** Components of the FE-HMM.

#### 4.2.2. Macro and Micro Finite Element Space

For the macro finite element space, the space  $\mathcal{V}^p(\mathcal{T}_H)$  with  $p = 1$  and the macrodecomposition  $\mathcal{T}_H$  of  $\Omega$  with step size  $H$ , as described in Section 4.1, is used. In the application, the step size  $H$  will be bigger than the width of the layers of the battery.

To define the micro finite element spaces, we need to describe microdomains. As shown in Figure 3 on each macroelement  $K \in \mathcal{T}_H$ , the Gauss quadrature points  $x_{K_j} \in K, j = 1, \dots, 4$ , are chosen and microdomains  $K_\delta(x_{K_j}) := x_{K_j} + \delta I$  with  $I = (-1/2, 1/2)^2$  and  $\delta > 0$  are defined.  $\delta$  will be described more precisely later.

Let  $\mathcal{T}_h$  be a decomposition of a microdomain  $K_\delta$  in quadrilaterals with step size  $h$ . In the application  $h$  will be smaller than  $H$ , especially much smaller than the width of the layers. Then the micro finite element space is

$$\mathcal{S}^1(K_\delta(x_{K_j}), \mathcal{T}_h) := \{z^h \in \mathcal{W}(K_\delta(x_{K_j})) : z^h|_T \in Q_1(T), \forall T \in \mathcal{T}_h\} \quad (22)$$

where  $\mathcal{W}(K_\delta(x_{K_j}))$  is the space  $\mathcal{H}^1$  on  $K_\delta(x_{K_j})$  with periodic boundary conditions. This space contains all functions which are continuous and square integrable over  $K_\delta(x_{K_j})$ , are bilinear on each element  $T$  of the decomposition  $\mathcal{T}_h$ , and fulfill a periodic boundary condition over  $K_\delta(x_{K_j})$ . The exact boundary conditions in Section 4.2.3 will complete the coupling of the problems.

#### 4.2.3. Microproblem

Now the microproblems are defined with whose solutions the macro bilinearform will be build. For each microdomain  $K_\delta(x_{K_j})$  let  $v_{K_j}^{h, a^\epsilon, s}$  be the solution of

$$\int_{K_\delta(x_{K_j})} a^\epsilon(x, s) \nabla v_{K_j}^{h, a^\epsilon, s}(x) \cdot \nabla z^h(x) dx = 0 \quad (23)$$

$$\forall z^h \in \mathcal{S}^1(K_\delta(x_{K_j}), \mathcal{T}_h)$$

with the boundary condition  $v_{K_j}^{h, a^\epsilon, s} - v_{\text{lin}, K_j}^H \in \mathcal{S}^1(K_\delta(x_{K_j}), \mathcal{T}_h)$ . Here,  $v_{\text{lin}, K_j}^H(x) = v^H(x_{K_j}) + (x - x_{K_j}) \cdot \nabla v^H(x_{K_j})$  is the linearization of the macrofunction  $v^H$  in  $x_{K_j}$  and  $s = u^H(x_{K_j})$  is the actual discrete solution at the quadrature node. This boundary condition couples the macro- and microproblem and shows how the microproblem depends on the macroproblem.

The solution of Equation (23) depends also on the coefficient  $a^\epsilon$ . This means that when the microproblems are solved,  $\lambda$  or  $c_p$  is inserted for  $a^\epsilon$ . In addition to the space variable, it depends also

on the actual discrete solution at the quadrature node, which leads to linear coefficients and not to nonlinear ones as  $\lambda$  and  $c_p$  are. This is permitted and justified by the fact that the coefficients are quasilinear. The benefit is that linear instead of nonlinear microproblems can be solved.

It is important to note that boundary conditions are only given for  $v_{K_j}^{h,a^e,s} - v_{\text{lin},K_j}^H$ . To solve Equation (23)  $\int_{K_\delta(x_{K_j})} a^e(x, s) \nabla v_{\text{lin},K_j}^H \cdot \nabla z^h(x) dx$  is subtracted from both sides of the equation and we arrive at

$$\begin{aligned} & \int_{K_\delta(x_{K_j})} a^e(x, s) \nabla (v_{K_j}^{h,a^e,s}(x) - v_{\text{lin},K_j}^H(x)) \cdot \nabla z^h(x) dx \\ &= \int_{K_\delta(x_{K_j})} a^e(x, s) \nabla v_{\text{lin},K_j}^H(x) \cdot \nabla z^h(x) dx \quad \forall z^h \\ & \in S^1(K_\delta(x_{K_j}), T_h) \end{aligned} \quad (24)$$

This is the problem that is actually solved. To get  $v^{h,a^e,s}, v_{\text{lin},K_j}^H$  is added to the solution.

As the step size  $h$  of the decomposition  $T_h$  is much smaller and the step size  $H$  of  $T_H$  is bigger than the microscale parameter, the domains  $K_\delta(x_{K_j}) \subset \Omega$  are the only domains where the microscale is resolved. So as mentioned in the introduction, what happens on the microscale is considered without resolving it everywhere. From that follows that fewer macro degrees of freedom—compared with the higher order FEM—are needed. In addition to that, as shown in the left part of Figure 3, the microproblems to different quadrature points are independent of each other. Therefore, the code is easily parallelizable and scales nearly perfectly, see [32], Section 4.1].

#### 4.2.4. Macro bilinearform

Now the bilinear form of Supporting Information B, Equation (18) will be modified using the microscale information. In the first steps, the decomposition of  $\Omega$  and a quadrature formula are used, which results in

$$\begin{aligned} B(T^{n+1}, \varphi) &= \\ & \sum_{K \in T_H} \left( \int_K \rho \frac{c_p(T^{n+1})T^{n+1} - c_p(T^n)T^n}{\Delta t} \varphi dx \right. \\ & \left. + \int_K \lambda(T^{n+1}) \nabla T^{n+1} \cdot \nabla \varphi dx \right) \\ & \approx \sum_{K \in T_H} \sum_{j=1}^4 \omega_{K_j}(\rho(x_{K_j})) \\ & \times \frac{c_p(T^{n+1}, x_{K_j})T^{n+1}(x_{K_j}) - c_p(T^n, x_{K_j})T^n(x_{K_j})}{\Delta t} \varphi(x_{K_j}) \\ & + \lambda(T^{n+1}, x_{K_j}) \nabla T^{n+1}(x_{K_j}) \cdot \nabla \varphi(x_{K_j}) \end{aligned} \quad (25)$$

Now the parts which consist of macrofunctions are replaced through integrals over the microdomains of the solutions of the appropriate microproblems and the modified bilinear form is defined with the solutions  $w_{K_j}^{h,(\cdot),u^H(x_{K_j})}$  and  $v_{K_j}^{h,(\cdot),u^H(x_{K_j})}$  of Equation (23) with appropriate coefficients and parameter  $s = u^H(x_{K_j})$  as

$$\begin{aligned} B_H(u^H; w^H, v^H) &:= \\ & \sum_{k \in T_H} \sum_{j=1}^4 \frac{\omega_{K_j}}{|K_\delta(x_{K_j})|} \left( \int_{K_\delta(x_{K_j})} \right. \\ & \times \rho \frac{c_p(u^H(x_{K_j})) w_{K_j}^{h,c_p,u^H(x_{K_j})} - c_p(T^{n,H}(x_{K_j})) T^{n,H}}{\Delta t} v_{K_j}^{h,c_p,u^H(x_{K_j})} dx \\ & \left. + \int_{K_\delta(x_{K_j})} \lambda(u^H(x_{K_j})) \nabla w_{K_j}^{h,\lambda,u^H(x_{K_j})} \cdot \nabla v_{K_j}^{h,\lambda,u^H(x_{K_j})} dx \right) \end{aligned} \quad (26)$$

Analogously to the derivation in Section 4.1, the matrix and right-hand side vector for the linear system can be defined. During the assembling of the matrix, the contributions from the microscale are computed “on-the-fly” on the corresponding macrocells. This saves computation time and memory. For more implementation aspects, see [32], Section 3].

#### 4.2.5. The Multiscale Method

With the help of Equation (26), the multiscale method is defined as follows. Find  $T^{n,H} \in \mathcal{V}^1(\Omega, T_H)$  with

$$B_H(T^{n,H}; T^{n,H}, v^H) = F(v^H) \quad \forall v^H \in \mathcal{V}^1(\Omega, T_H) \quad (27)$$

where  $F(v^H)$  is the linear form in Supporting Information B, Equation (19). The nonlinearities of the macroproblem are resolved with the undamped Newton method which results for the Newton update  $\delta T_k^{n,H}$  with the actual solution  $T_k^{n,H}$  in

$$\begin{aligned} \partial_T B_H(T_k^{n,H}; T_k^{n,H}, v^H) - F(T_k^{n,H}; v^H) [\delta T_k^{n,H}] \\ = -B_H(T_k^{n,H}; T_k^{n,H}, v^H) - F(T_k^{n,H}; v^H) \quad \forall v^H \in \mathcal{V}^1(T_H) \end{aligned} \quad (28)$$

The linear system resulting from this equation is solved with the CG algorithm.

## 5. Results

In the previous two sections, altogether six different methods—the chtMultiRegionFoam, the layeredLaplacianFoam, three higher order FEMs, and the FE-HMM—were introduced to solve Equation (1). In Section 5.1, an error analysis including the demonstration of optimal convergence order for the FE-HMM will be shown. This will be done based on a stationary test problem with multiple multiscale coefficients. After that the application of this method to the battery problem will be presented. In Section 5.2, the convergence of the other five methods will be shown, their order of convergence will be computed, and they will be compared regarding computation time and scaling with regard to parallelization. For that a stationary elliptic test problem with a discontinuous coefficient will be used. One reason for the necessity of different test problems is that for the FE-HMM a problem with multiscale coefficients is needed. Even if this would be used for testing the other five methods, their results would not converge to a homogenized solution as the FE-HMM does, but to the unhomogenized solution, which would make the comparison of all methods impossible. In Section 5.3, all six methods will be applied to the thermal battery problem.

## 5.1. Results for the FE-HMM

### 5.1.1. Error Analyses

An important mathematical feature of the FE-HMM introduced in the last section is that there exist a priori error estimates. That guarantees that the method converges to the desired solution. The aim is to characterize  $\|T^0 - T^H\|$ , where  $T^0$  is the exact solution of the homogenized problem,  $T^H$  is the solution of Equation (27), and the norm is the  $\mathcal{H}^1$  or the  $\mathcal{L}^2$  norm, which are defined for a function  $f: \Omega \rightarrow \mathbb{R}$  as follows

$$\|f\|_{\mathcal{L}^2(\Omega)} := \left( \int_{\Omega} |f(x)|^2 dx \right)^{\frac{1}{2}}, \quad (29)$$

$$\|f\|_{\mathcal{H}^1(\Omega)} := \left( \|f\|_{\mathcal{L}^2(\Omega)}^2 + \|\nabla f\|_{\mathcal{L}^2(\Omega)}^2 \right)^{\frac{1}{2}}$$

It was shown in [19], Section 3.3] and [30], Section 3] that for the problem with one multiscale coefficient the error estimates

$$\|T^0 - T^H\|_{\mathcal{L}^2(\Omega)} \leq C(H^2 + (h/\epsilon)^2) \quad (30)$$

$$\|T^0 - T^H\|_{\mathcal{H}^1(\Omega)} \leq C(H + (h/\epsilon)^2) \quad (31)$$

hold. It will be confirmed numerically later that the results are equally valid in the case of multiple multiscale coefficients. From Equation (30) and (31) follows that optimal convergence rates are achieved if the macro- and microgrid are refined simultaneously in the  $\mathcal{L}^2$  case and according to  $h \sim \sqrt{H}$  in the  $\mathcal{H}^1$  case. The sharpness of the estimates is illustrated on the following equation, which is based on the example in [30], Section 5] and has the same structure as Equation (16) in Supporting Information B for a fixed time. To consider such a case is sufficient because it is known that the implicit Euler method converges with order one in time.

$$-\nabla \cdot (a^\epsilon(x, u^\epsilon(x)) \nabla u^\epsilon(x)) + b^\epsilon(x, u^\epsilon) u^\epsilon(x) = f(x) \quad (32)$$

$$\forall x \in \Omega = [0, 1]^2$$

$$u^\epsilon(x) = 0 \quad \forall x \in \partial\Omega \quad (33)$$

with the  $\epsilon$ -dependent coefficients

$$a^\epsilon(x, s) = \frac{1}{\sqrt{3}} \begin{pmatrix} (2 + \sin(\frac{2\pi x_1}{\epsilon}))(1 + \sin(\pi s)) & 0 \\ 0 & (2 + \sin(\frac{2\pi x_2}{\epsilon}))(2 + \arctan(s)) \end{pmatrix} \quad (34)$$

$$b^\epsilon(x, s) = \left( 1 + \cos\left(\frac{4\pi x_1}{\epsilon}\right) \right) (2 + x_1 \cos(\pi s)) \quad (35)$$

and a right-hand side  $f$  that is chosen in such a way, that  $u^0(x) := 8 \sin(\pi x_1) x_2 (1 - x_2)$  is the exact solution of the homogenized equation

$$-\nabla \cdot (a^0(x, u^0(x)) \nabla u^0(x)) + b^0(x, u^0(x)) u^0(x) = f(x) \quad (36)$$

$$\forall x \in \Omega$$

$$u^0(x) = 0 \quad \forall x \in \partial\Omega \quad (37)$$

Here, the homogenized coefficients  $a^0$  and  $b^0$  are explicitly computable as

$$a^0(x, s) = \begin{pmatrix} 1 + x_1 \sin(\pi s) & 0 \\ 0 & 2 + \arctan(s) \end{pmatrix} \quad (38)$$

$$b^0(x, s) = 2 + x_1 \cos(\pi s) \quad (39)$$

For the computations  $\epsilon = 10^{-4}$  is chosen. This is sufficient because the smallest  $H$  will be much bigger than that. **Figure 4** shows the relative  $\mathcal{L}^2$  error, i.e. the error divided by the norm of the solution, when either  $H$  (Figure 4a) or  $h$  (Figure 4b) is refined and the other parameter is kept fixed. The error is plotted for  $h, H = 1/2, 1/4, 1/8, 1/16, 1/32$ . It can be observed that optimal convergence rates are only reached if the macro- and micromeshes are refined simultaneously. In the other cases, one part of the errors shown in Equation (30) and (31), respectively, dominates the other. This is shown for the  $\mathcal{L}^2$  and for the  $\mathcal{H}^1$  error in Figure 4c. Here, optimal convergence rates are observed as stated in Equation (30) and (31).

### 5.1.2. Application to the Battery Problem and Implementation Aspects

Now the previous sections will be summarized and the specific application of the method to problem of Equation (1) on the modeled battery geometry will be shown.

In **Figure 5**, a segment of the geometry is seen, which is the mathematical macrodomain  $\Omega$ . The macrostep size  $H$  is chosen so that it is 2 times the width of the active material and the width of each current collector layer. With this choice the resolution of all layers is avoided, as it was done in Section 4.1. The microscale parameter  $\epsilon$  is the sum of the dimensionless thicknesses of the three different layers. As it was pointed out at the beginning of the section, the discontinuous periodic material coefficients are the multiscale coefficients  $a^\epsilon, b^\epsilon$ .

As stated in Section 4.2.1, the Gauss quadrature with two quadrature points in each direction is chosen, i.e. that there are four quadrature points in each macrocell as it is shown in the middle part of Figure 5. Around them the microdomains  $K_{\delta_j}$  are taken in a way that they contain parts from the active material layers and from the current collector layers. This guarantees that both types of layer are considered. If the equation would be solved with finite elements with step size  $H$  in the case of the two-point Gauss quadrature rule, the coefficients would only be evaluated in the active material layers, as it can be seen in the middle part of Figure 5. This means that only an equation with just one broad active material layer and no current collector layers would be solved.

In the microdomains, a decomposition with step size  $h$  is used which is small enough to sufficiently resolve the layers. In Section 4.1, the step size of the entire decomposition was roughly as small because there the layers had to be resolved everywhere.

## 5.2. Test Problem

To compare the two OpenFOAM methods and the higher order FEM as a test problem, a steady-state diffusion problem

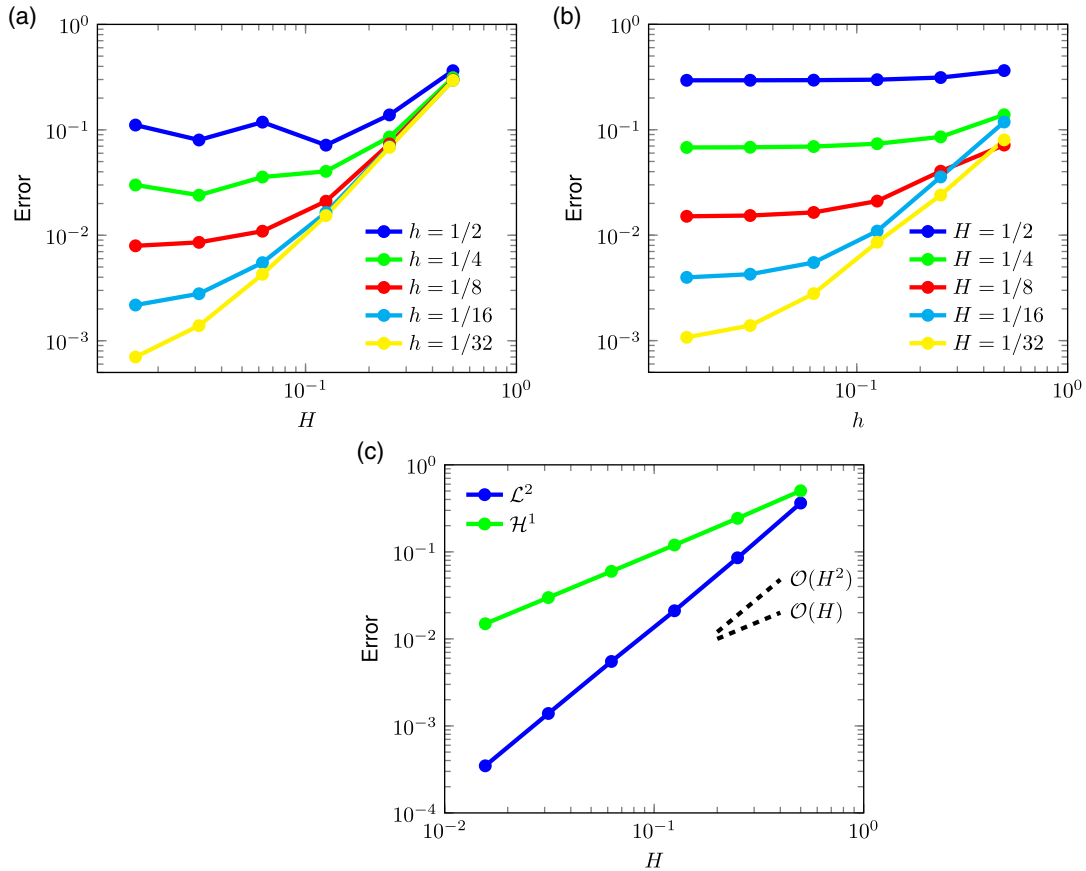


**Figure 4.** Convergence rates of the FE-HMM for different refinements. a)  $L^2$  errors of the FE-HMM for  $H$ -refinement for fixed  $h$ . b)  $L^2$  errors of the FE-HMM for  $h$ -refinement for fixed  $H$ . c) Errors for simultaneous refinement of  $h = H$ .

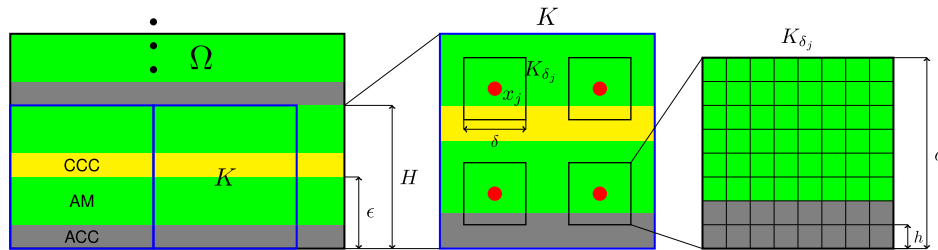


**Figure 5.** Application of the FE-HMM.

with discontinuous coefficients is considered. Such a problem can be seen similar to a spatial segment of one time step of the battery problem. This is sufficient for the comparison because on the one side only the convergence of the methods will be demonstrated and the order of convergence for problems with such coefficients will be shown and on the other side for the battery problem the time steps will be chosen in a way that the error is dominated by the spatial error and not by the error caused by time discretization. So the following problem for a given  $s \in (0, \pi)$  is considered

$$-\nabla \cdot (a_s(x) \nabla u(x, \gamma)) = f(x, \gamma) \quad \forall (x, \gamma) \in \Omega := [0, \pi]^2 \quad (40)$$

$$u(0, \gamma) = u_{\text{ex}}(0, \gamma) \quad (41)$$

$$u(\pi, \gamma) = u_{\text{ex}}(\pi, \gamma) \quad (42)$$

$$a_s(x) \partial_\gamma u(x, 0) = a_s(x) \partial_\gamma u(x, \pi) = 0 \quad (43)$$

with

$$a_s(x) = \begin{cases} a_1 := 1, & x < s \\ a_2 := 10, & x \geq s \end{cases} \quad (44)$$

and  $f(x, \gamma) = a_s(x) \sin(x)$ . This  $f$  is chosen such that the equation has the exact analytical solution

$$u_{\text{ex}}(x, \gamma) = \begin{cases} \sin(x) + c_1(s)x, & x < s \\ \sin(x) + c_2(s)(\pi - x), & x \geq s \end{cases} \quad (45)$$

where the real coefficients  $c_1(s)$  and  $c_2(s)$  are chosen such that the solution and the fluxes  $a_i \partial_x u$  are continuous in  $s$ . Results for  $s = \pi/2$  and  $s = \pi/3$  will be presented. Furthermore, the choice for these values for  $s$  will be explained. For both setups, the problem is solved with the CG algorithm for a tolerance  $\text{tol} = 10^{-12}$  and without parallelization. Under the above assumptions  $c_1(\pi/2) = c_2(\pi/2) = 0$  for  $s = \pi/2$  and  $c_1(\pi/3) = 0.75$ ,  $c_2(\pi/3) = 0.375$  for  $s = \pi/3$  are found.

All computations were done on the single partition of the BwUniCluster 2.0.<sup>[33]</sup> The computation times are the averages of three runs to reduce the impact of deviations on the results caused by the cluster. For the error and time measurements  $N = 8, 16, 32, \dots, 1024$  cells per dimension are considered, no parallelization is used and a preconditioner is only applied for the time measurement of the FEM with  $p = 2$  and  $p = 3$ . For the investigation of the scaling of the solvers with respect to parallelization  $n = 1, 2, 4, \dots, 32$  cores were used. In the plots  $p \in \{1, 2, 3\}$  stands for the finite element solver with the respective order, ILF stand for layeredLaplacianFoam and CHT for chtMultiRegionFoam.

At first, a look at the errors for the two different  $s$  values is taken. According to <sup>[26]</sup>, Section 2.7] for the solution  $u^h$  of the FEM of order  $p$  for a sufficiently regular solution  $u$ , the estimates

$$\|u - u^h\|_{L^2(\Omega)} \leq Ch^{p+1}, \quad \|u - u^h\|_{L^\infty(\Omega)} \leq Ch^{p+1} \quad (46)$$

with a constant  $C > 0$  are fulfilled, where  $h = 1/N$  is the cell size. If the solution, its gradient, and the gradient of the right-hand side are bounded, then according to <sup>[27]</sup>, Section 9.4] the finite volume solution shows the error bounds

$$\|u - u^h\|_{L^2(\Omega)} \leq Ch, \quad \|u - u^h\|_{L^\infty(\Omega)} \leq Ch \quad (47)$$

where the  $L^2$  norm is defined in Equation (29) and the  $L^\infty$  norm of a continuous function  $f$  is defined as follows

$$\|f\|_{L^\infty(\Omega)} := \max_{x \in \Omega} |f(x)| \quad (48)$$

This means that for the FEM solutions  $p + 1$  and for the two FVM solutions 1 as the order of convergence is expected.

As shown in **Figure 6a,b**, these bounds can be observed in the case of  $s = 0.5\pi$ . The two FVM solutions converge with order 1

and the FEM solutions with  $p + 1$ . For  $p = 3$  it is observed that the error cannot improve further below  $10^{-11}$ , which is less than what is needed in practice. For these computations, the tolerance  $10^{-12}$  is used for the CG method, but the result will still be the same for  $10^{-15}$ . Thus, this effect is due to the occurrence of rounding errors. It can be concluded that all of the methods show optimal convergence rates.

When observing the errors in the case  $s = 1/3\pi$  in **Figure 7a,b**, it can be seen that the errors of all methods have the same magnitude. Moreover, it can be recognized that they all converge, but only the solutions of the FVMs converge with the theoretical optimal order, while all the solutions of the FEMs are limited to an order around one. The reason for this behavior lies in the regularity of the solution. Optimal convergence rates for the FEM (or the FVM as well) are only reached, if the solution of the problem is sufficiently regular. This is only the case for  $s = 0.5\pi$  because in that case for all  $\gamma \in [0, \pi]$   $\partial_x u_{\text{ex}}(0.5\pi, \gamma) = \cos(0.5\pi) = 0$  and so

$$\begin{aligned} & -\nabla(a_{0.5\pi}(0.5\pi)\nabla u_{\text{ex}}(0.5\pi, \gamma)) \\ &= -a_{0.5\pi}(0.5\pi)\Delta u_{\text{ex}}(0.5\pi, \gamma) + \partial_x a_{0.5\pi}(0.5\pi)\partial_x u_{\text{ex}}(0.5\pi, \gamma) \\ &= -a_{0.5\pi}(0.5\pi)\Delta u_{\text{ex}}(0.5\pi, \gamma) + (a_2 - a_1)\delta_{0.5\pi}\partial_x u_{\text{ex}}(0.5\pi, \gamma) \\ &= -a_{0.5\pi}(0.5\pi)\Delta u_{\text{ex}}(0.5\pi, \gamma) \end{aligned} \quad (49)$$

where  $\delta$  is the Dirac measure. This means that in this case the jump of the coefficient is invisible. This is not the case for all other  $s$ -values, especially  $s = 1/3\pi$ . Here, the solution is continuous, but not continuously differentiable, and so lacks regularity to observe higher order convergence than 1. As for the finite volume case all requirements are fulfilled, an average order of one is reached. This leads to the conclusion that in the case of discontinuous coefficients an optimal order of convergence can only be expected in cases where additional requirements are fulfilled.

Moreover, it can be observed that the  $L^2$  and the  $L^\infty$  error show a zigzag shape. The reason for that lies in the position of the discontinuity of the coefficient in the grid. In this case it is  $x = \pi/3$ , which will never exactly coincide with cell boundaries and so two classes of decompositions are created. In one of them all quadrature points of the cells at  $\pi/3$  belong to the same part of the domain and in the other  $\pi/3$  separates them. These classes belong to every second point in **Figure 7a,b**, respectively, and each of them depicts an optimal convergence behavior.

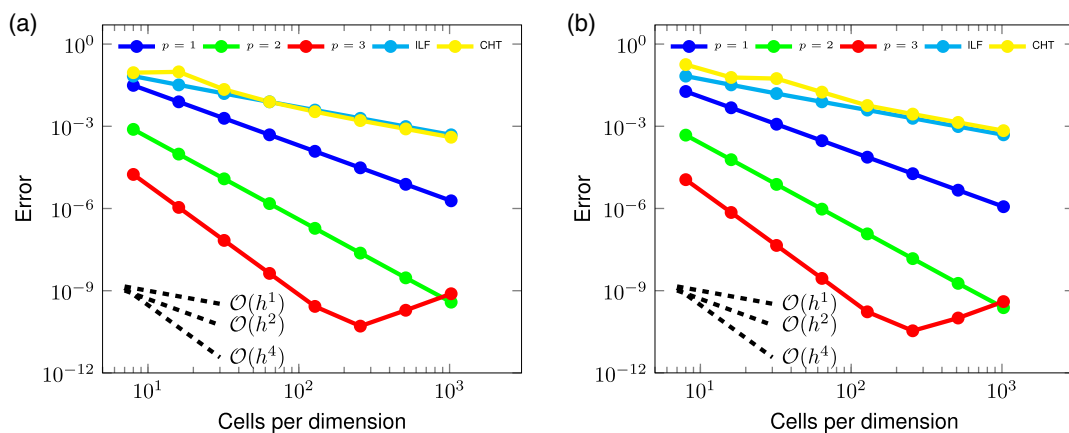


**Figure 6.** Errors of the different methods for  $s = 0.5\pi$ . a)  $L^2$ -error. b)  $L^\infty$ -error.

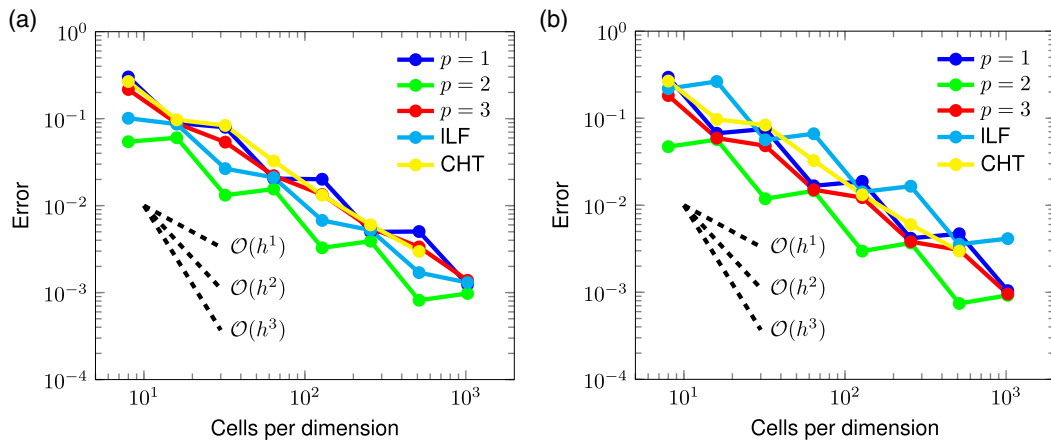


**Figure 7.** Errors of the different methods for  $s = 1/3\pi$ . a)  $L^2$ -error. b)  $L^\infty$ -error.

Further it can be seen that for  $x = \pi/3$  the error of the  $p = 3$  case is not lower as that of the  $p = 2$  case. This is due to the irregularity of the problem. For such a problem, the FEMs of different order provide similar errors. The reason for that is again the location of the quadrature points as a Gauss quadrature of order  $p + 1$  is used. For the  $p = 2$  case, their positions are advantageous which results in a lower error.

With regard to the battery problem, which also has discontinuous coefficients, this means that all of the methods will converge, but statements about the order of convergence cannot be made because the problem has no explicitly known analytical solution.

Until now, only the errors of the methods were examined, but no care was taken of the computation time, i.e. how long does it take to achieve a given accuracy. **Figure 8a** shows the computation times of the methods. At first it can be observed that chtMultiRegionFoam has two order of magnitude higher computation times for the highest resolution than the other methods. The reason for that lies in the structure of the solver. As mentioned in Section 3.1, it needs several loops to arrive at the solution and these loops take more time. The layeredLaplacianFoam has similar computation times as the

FEM with  $p = 1$ . This was expected because they have nearly the same number of degrees of freedom, they do not need any additional loops, as the chtMultiRegionFoam does, and they use the same CG algorithm.

As mentioned in the first part of this section, a preconditioner was only used for the cases  $p = 2$  and  $p = 3$ . This results in similar computation times to case  $p = 1$ , despite the fact that they have 4 and 9, respectively, times more degrees of freedom. This leads to another important aspect of the methods which, however, is not addressed any further in this work. This is the influence of the preconditioners. Moreover, it is observed that the methods without a preconditioner, except the FVMs for small number of cells, scale cubically, or in the case of chtMultiRegionFoam even faster, in the number of cells in one spatial dimension, where the methods with a preconditioner scale quadratically.

The reason for the nearly constant computation times for the FVMs for a small number of cells is that apart from the assembling of the matrix and solving the linear system the generation of the output is included, too. For small cell numbers, the generation of the output dominates the computation time in OpenFOAM.

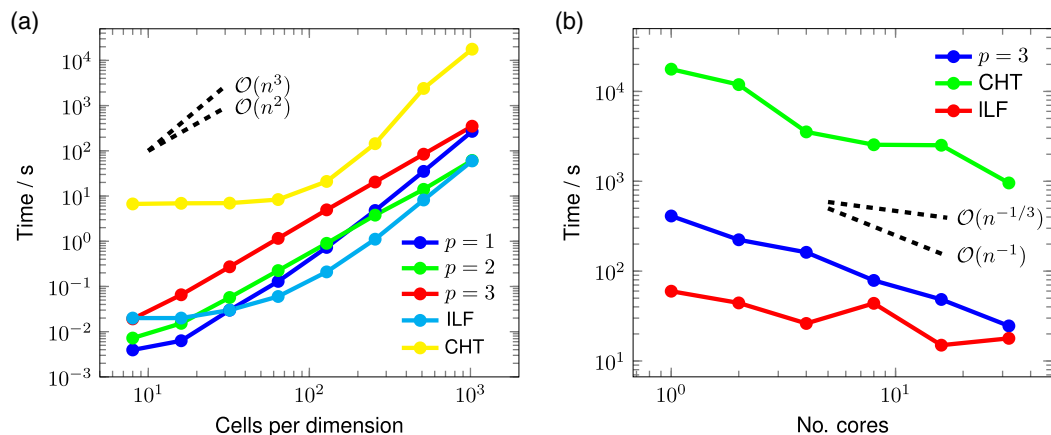


**Figure 8.** a) Comparison of the computation time and b) scaling of the methods.

The last aspect that is examined at the test problem is the scaling regarding parallelization. The results are shown in Figure 8b. Because all FEMs have the same structure, only the case  $p = 3$  is compared with the FVMs. It is observed that the chtMultiRegionFoam and the FEM scale nearly optimal, i.e. if the number of cores is doubled, the computation time nearly halves, which is the best that can be expected. In the case of the layeredLaplacianFoam, only a small reduction is observed.

### 5.3. Battery Problem

Now the six methods are applied to the linear 2D version of problem (cf. Equation (1)), i.e.  $\Omega \subset \mathbb{R}^2$  and  $c_p$  and  $\lambda$ , respectively, be temperature independent. The integral heat source is again set to overall 3 W in the active material layers and in the current collectors to 0 W. A period of  $t_{\text{end}} = 10$  s with a time step  $\Delta t = 0.01$  s will be simulated again on 32 cores of the single partition of the BwUniCluster 2.0.<sup>[33]</sup> As stated in Section 2,  $T_{\text{init}} = 298$  K will be used as initial condition and the following three boundary value problems will be considered: 1) Dirichlet boundary condition with  $T_{\text{BC}} = 273$  K at the lower side of the cell; 2) Robin boundary condition with  $T_{\text{BC}} = 273$  K and  $a = 10 \text{ W m}^{-2} \text{ K}^{-1}$  at the lower side of the cell; and 3) Dirichlet boundary condition with  $T_{\text{BC}} = 273$  K at the left and right side of the cell; where in all cases a zero Neumann boundary condition will be applied to all other sides of the battery. In the following figures, HMM stands for the solution of the problem with FE-HMM.

To compare the six methods, a reference solution with FEM of order  $p = 3$  and with about 5 million degrees of freedom is computed. Regarding the discussions in Section 5.2, this method gives the most accurate numerical solution among those presented here. At first, the reference solution for the three boundary value problems will be presented. Then the six methods will

be compared based on the reference solution and along chosen lines in space and time. Finally, the computation times of the solvers will be compared. For all the comparisons, the case with Dirichlet boundary condition at the lower side of the battery is chosen. All other cases would yield similar results because the boundary condition does not change the structure of the methods. All methods, except the FE-HMM, use a grid of around 150 000 cell elements.

Figure 9 shows the temperature distribution in the  $yz$ -plane after 10 s for a Dirichlet boundary condition on the lower side of the cell calculated with chtMultiRegionFoam. For the Dirichlet boundary condition 273 K is applied while the initial temperature is 298 K. Obviously, a temperature gradient forms with the lowest temperature at the lower boundary and increasing in  $z$ -direction up to 298 K at the upper side. In  $y$ -direction, no difference can be recognized.

The temperature gradient is caused by the thermal transport to the heat sink at the lower boundary. Apart from the stack, no further battery component is mapped in the geometry, which could induce a thermal bypass path, as shown in Queisser et al.<sup>[7]</sup> This aspect and the adiabatic boundary conditions at the both front sides of the cell lead to the result that no temperature gradient develops in  $y$ -direction.

In summary, the results for chtMultiRegionFoam and also for the other methods, shown in Figure 9 as well as the two further cases presented in Supporting Information C, are physically reasonable, which again supports the plausibility of the methods.

For the comparison of the methods in space and time, a Dirichlet boundary condition on the lower side of the cell is used. The spatial comparison is done along a vertical line in the middle of the cell. This choice is justified by the fact that in the considered case a zero Neumann boundary condition at the left and right side of the battery is used, which results in a constant temperature along a horizontal line, as it can be seen in Figure 9. Figure 10 shows the temperature distribution at time  $t = 1$  s

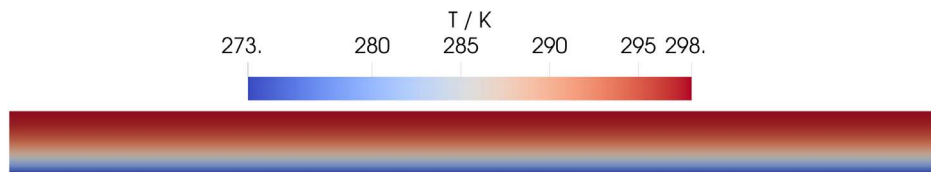


Figure 9. Temperature distribution of the cell stack for a Dirichlet boundary condition at lower side of the cell after 10 s solved with chtMultiRegionFoam.

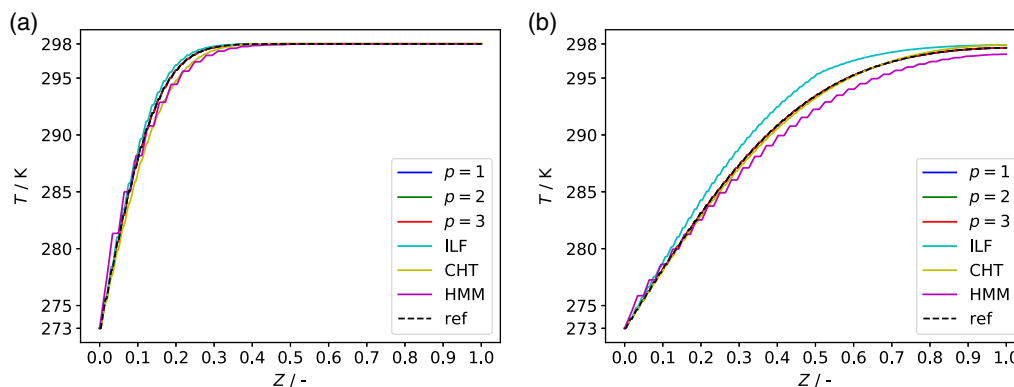


Figure 10. Temperature distribution over a vertical line through the middle of battery. a)  $t = 1$  s. b)  $t = 9$  s.

and at  $t = 9$  s, respectively. First, it can be observed that all methods capture the steps in the temperature distribution which occur due to the discontinuities of the coefficients. These steps are bigger in the case of the FE-HMM because there a coarser grid is used. Moreover, it can be seen that at time  $t = 1$  s all methods are in good agreement with the reference solution, the FEM solutions lie even on top of it, and the maximal deviation is smaller than 1%, which occurs for the FE-HMM solution. One reason for that is that this solution converges to the solution of the mathematically homogenized problem, as mentioned in Section 4.2, so a complete agreement cannot be expected. The other reason for that is that this method uses only a fraction of the number of cells than the other methods and so near the boundary, where the gradient of the solution is higher, the difference is bigger. With time these gradients get smaller and so the error of the FE-HMM solution gets smaller, too. At time  $t = 9$  s it is only around 0.5%. The solutions with FEMs and the solution of the chtMultiRegionFoam are for both times in good agreement with the reference solution; the deviations are nearly negligible. This is in agreement with the results of the test problem in Section 5.2. The reason is that all methods, including the reference solution, use the implicit Euler method with the same time step for the temporal discretization and so the error results mainly from the spatial discretization. The only method where the error gets bigger with time is the layeredLaplacianFoam, but also its maximum is only around 1%, which is acceptable.

Figure 11 shows how the error of the methods compared with the reference solution propagates over time at fixed points in space. It is observed that the solutions of the FEMs and the solution of the chtMultiRegionFoam are for both points in good agreement with the reference solution; they nearly lie on top of it, i.e. that the error does not accumulate over time. The reason for that is the same as explained earlier. The error of the layeredLaplacianFoam is again bigger, but again only around 1%.

The last aspect, which is considered here, is again the computation time. The results for the first five time steps are shown in Table 2. This shows that the results for the FEM and FVM solutions of the battery problem are in agreement with the results for the test problem, as shown in Figure 8a. This means that the chtMultiRegionFoam has due to the loops higher computation times than the other methods and the layeredLaplacianFoam is faster than the preconditioned FEMs

**Table 2.** Average computation times of the first five time steps for each method.

	$p = 1$	$p = 2$	$p = 3$	ILF	CHT	HMM
Time	1.04 s	4.83 s	15.03 s	1.5 s	54.14 s	2.67 s

with  $p = 2$  and  $p = 3$ . In the case that a preconditioner is used for the  $p = 1$  case too, it is observed that it is faster than layeredLaplacianFoam. The computation time of the FE-HMM is approximately the same as that of the layeredLaplacianFoam. The reason is that although it has a smaller number of cells and so a smaller system matrix, the microsimulations take time, too. It is important to note that Table 2 only shows the times needed for the first five time steps. As these times depend mainly on the number of CG steps needed for the actual time step, they can change in time. Figure 10 shows smaller changes in the solution in  $z$ -direction with time. As a consequence, this results in a decreasing number of CG steps and thus the relations shown in Table 2 remain valid.

## 6. Summary and Conclusion

In this work, different numerical methods for the thermal simulation of the layered stack of lithium-ion batteries were introduced and investigated. This stack consists of a large number of thin layers, which leads to two possible approaches for the applied methods. On the one hand, the standard approach was considered. There, all layers were resolved with methods based on standard numerical techniques such as the FEM and the FVM. Higher order FEMs with  $p = 1, 2, 3$  implemented in the finite element library deal.II, the chtMultiRegionFoam, and the self-developed layeredLaplacianFoam in OpenFOAM were considered. On the other hand, a homogenization approach was followed. A numerical method, the FE-HMM, was implemented in deal.II, extended, and applied to the problem, which solves it without resolving all layers with sufficient efficiency.

At first the convergence behavior of the altogether six methods were examined on the basis of appropriate test problems. It was shown that the FE-HMM converges with optimal order in the

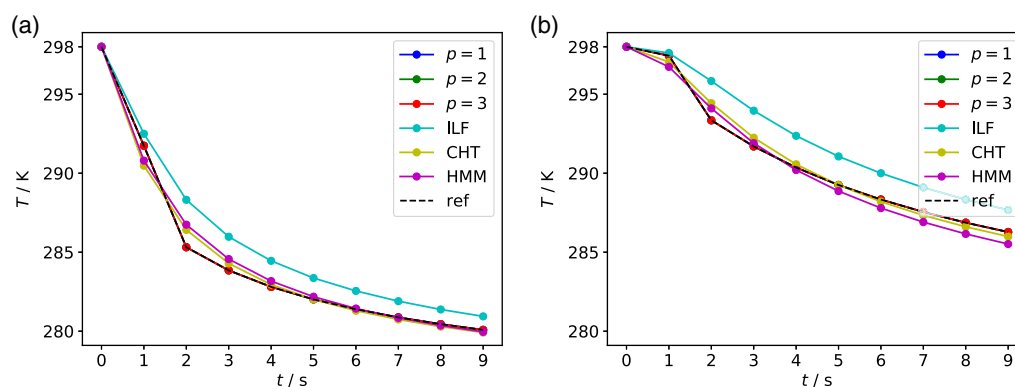


**Figure 11.** Temperature distribution for a given point in the middle of the battery over time. a)  $Z = 0.134$ . b)  $Z = 0.268$ .

case of appropriate refinement for problems with multiple multiscale coefficients, such as the heat equation, which describes the thermal behavior of the battery. For any higher order method, the optimal order of convergence can only be expected when the solution satisfies additional regularity assumptions. If these assumptions are not met, the optimal order of convergence in terms of unknowns can be obtained when a posteriori error controlled  $h$ -refinement is performed.<sup>[34]</sup> This means that results for problems with unknown regularity have to be examined carefully. For the methods based on the FVM, weaker assumptions on the solution are required, which leads to an optimal convergence order in the case of discontinuous coefficients, too. This has the consequence that, regarding the error, the theoretically better FEMs lose their advantage for the problem considered here, at least, without local mesh refinement techniques.

Comparing the computation times it was observed that `chtMultiRegionFoam` has much higher computation times than the other methods because of the loops resulting from its structure. On the basis of the FEM cases  $p = 2$  and  $p = 3$ , respectively, it could be observed that other development aspects, such as preconditioners, play an important role as well. In this regard, the scaling behavior of the methods regarding parallel application was considered, too. As most of the considered methods resolve all layers of the battery, they have a huge number of cells and degrees of freedom, for that parallelization is inevitable. It turned out that all methods except the `layeredLaplacianFoam` scale nearly perfectly. Altogether, it is hard to evaluate the methods with regard to computation time because many different aspects have to be considered.

Finally, the investigated methods were then applied to the battery problem with different boundary conditions. To be able to compare them, a reference solution with a higher resolution was computed. It was observed that, as expected on the basis of the test problem, all methods converge along chosen lines in space and at specified points over time. The computation times for the battery are in agreement to what was observed for the test problem. It is important to note that, since FE-HMM is a homogenization method, its benefit regarding computation time rises with the number of layers in the battery.

In future work, on the one hand, an electrical model should be coupled to the existing thermal model. While the efficiency gain by the current method already supports the practical feasibility of such coupled electrothermal simulations, further improvement of the computing time will allow for long-term simulations, potentially even for aging modeling. On the other hand, the applied numerical schemes and the errors from resolving the time derivative should be investigated in more depth and the FE-HMM should be adapted to facilitate using it in FVM.

On the basis of the aforementioned considerations and discussions, it can be concluded that there are a lot of possibilities for the simulation of thermal processes in batteries, but apart from the modeling the development and the rigorous investigation of the numerical methods used for the simulations are very important. As shown on the example of the test problem, the lack of that can lead to insufficient convergence behavior and long computation times.

## Supporting Information

Supporting Information is available from the Wiley Online Library or from the author.

## Acknowledgements

M.G., O.Q., and Z.V. acknowledge financial support by the German Research Foundation (DFG) through RTG 2218 SiMET—simulation of mechano-electro-thermal processes in lithium-ion batteries, project number 281041241. Open access funding enabled and organized by Projekt DEAL.

## Conflict of Interest

The authors declare no conflict of interest.

## Keywords

heterogeneous multiscale method, lithium-ion batteries, numerical methods, temperature distribution, thermal modeling

Received: October 15, 2020

Revised: November 9, 2020

Published online:

- [1] D. Werner, S. Paarmann, A. Wiebelt, T. Wetzel, *Batteries* **2020**, 6, 13.
- [2] D. Werner, S. Paarmann, A. Wiebelt, T. Wetzel, *Batteries* **2020**, 6, 1.
- [3] T. M. Bandhauer, S. Garimella, T. F. Fuller, *J. Electrochem. Soc.* **2011**, 158, 3.
- [4] S. Goutam, A. Nikolian, J. Jaguemont, J. Smekens, N. Omer, P. V. D. Bosche, J. V. Mierlo, *Appl. Therm. Eng.* **2017**, 126, 796.
- [5] M. Guo, R. E. White, *J. Power Sources* **2012**, 221, 334.
- [6] S. Allu, S. Kalnaus, W. Elwasif, S. Simunovic, J. A. Turner, *J. Power Sources* **2014**, 246, 876.
- [7] O. Queisser, L. Cloos, F. Boehm, D. Oehler, T. Wetzel, *Energy Technol.* **2020**, <https://doi.org/10.1002/ente.202000915>.
- [8] X. Ciu, J. Zeng, H. Zhang, J. Yang, J. Qiao, J. Lie, W. Li, *Int. J. Energy Res.* **2020**, 44, 3640.
- [9] G. Liebig, U. Kirstein, S. Geißendörfer, F. Schuldt, C. Agert, *Batteries* **2020**, 6, 1.
- [10] S. Chen, C. Wan, Y. Wang, *J. Power Sources* **2005**, 240, 111.
- [11] M. J. Hunt, F. B. Planelle, F. Theil, W. Widanage, *J. Eng. Math.* **2020**, 122, 31.
- [12] M. G. Hennessy, I. R. Moyles, *Appl. Math. Modell.* **2020**, 80, 724.
- [13] G.-H. Kim, K. Smith, K.-J. Lee, S. Santhanagopalan, A. Pesaran, *J. Electrochem. Soc.* **2011**, 8, A955.
- [14] Y. Efendiev, T. Y. Hou, *Multiscale Finite Element Methods*, Springer, Berlin/New York **2009**.
- [15] A. Quarteroni, A. Manzoni, F. Negri, *Reduced Basis Methods for Partial Differential Equations*, Springer, Berlin/New York **2016**.
- [16] W. E. B. Engquist, *Commun. Math. Sci.* **2003**, 1, 87.
- [17] W. E. B. Engquist, X. Li, W. Ren, E. Vanden-Eijnden, *Commun. Comput. Phys.* **2007**, 2, 367.
- [18] A. Abdule, C. Schwab, *Multiscale Model. Simul.* **2005**, 3, 195.
- [19] A. Abdule, *GAKUTO Int. Ser., Math. Sci. Appl.* **2009**, 31, 133.
- [20] P. Ming, P. Zhang, *Math. Comp.* **2007**, 76, 153.
- [21] A. Abdule, M. Huber, *ESAIM: Math. Modell. Numer. Anal.* **2016**, 50, 1659.

- [22] D. Bernardi, E. Pawlikowski, J. Newman, *J. Electrochem. Soc.* **1985**, 132, 1.
- [23] P. Stephan, S. Kabelac, M. Kind, D. Mewes, K. Schaber, T. Wetzel, *VDI-Wärmeatlas*, Vol. 12, Springer, Berlin/New York **2019**.
- [24] C. Greenshields, OpenFOAM v6 User Guide, The OpenFOAM Foundation, <https://cfd.direct/openfoam/user-guide> (accessed: October 2020).
- [25] J. Ferziger, M. Perić, *Numerische Strömungsmechanik*, Springer, Berlin/New York **2008**.
- [26] D. Braess, *Finite Elemente: Theorie, schnelle Löser und Anwendungen in der Elastizitätstheorie*, Springer-Verlag, Berlin/Heidelberg **2013**.
- [27] A. Quarteroni, *Numerical Models for Differential Problems*, Springer, Berlin/New York **2017**.
- [28] M. Schatzman, *Numerical Analysis*, Clarendon Press, Oxford **2002**.
- [29] D. Cioranescu, P. Donato, *An Introduction to Homogenization*, Oxford University Press, Oxford **1991**.
- [30] A. Abdulle, G. Vilmart, *Math. Comput.* **2014**, 83, 513.
- [31] W. E. P. Ming, P. Zhang, *J. Am. Math. Soc.* **2005**, 18, 121.
- [32] A. Abdulle, A. Nonnenmacher, *Comput. Methods Appl. Mech. Eng.* **2009**, 37, 2839.
- [33] Bwunicluster 2.0, [https://wiki.bwhpc.de/e/Category:BwUniCluster\\_2.0](https://wiki.bwhpc.de/e/Category:BwUniCluster_2.0) (accessed: October 2020).
- [34] R. Stevenson, *Found. Comput. Math.* **2007**, 7, 245.
- [35] F. Moukalled, L. Mangani, M. Darwish, *The Finite Volume Method in Computational Fluid Dynamics*, Springer, Berlin/New York **2016**.
- [36] P. Ciarlet, *Handbook of Numerical Analysis*, Vol. 7, Springer, Berlin/New York **2000**.
- [37] J. Qvist, in *CFD with OpenSource Software* (Ed: H. Nilsson), [http://dx.doi.org/10.17196/OS\\_CFD#YEAR\\_2019](http://dx.doi.org/10.17196/OS_CFD#YEAR_2019) **2019**.
- [38] D. Gallistl, C. Stohrer, Numerical Multiscale Methods, Technical Report, KIT, Institute for Applied and Numerical Mathematics **2017**.